Journal of Microscopy, Vol. 215, Pt 3 September 2004, pp. 271–280
Received 5 February 2004; accepted 27 April 2004

Simulation of specimen-induced aberrations for objects with spherical and cylindrical symmetry

M. SCHWERTNER, M. J. BOOTH & T. WILSON
Department of Engineering Science, University of Oxford, Parks Road, Oxford OX1 3PJ, U.K.

Key words. Aberration simulation, adaptive optics, confocal and multiphoton microscopy, interferometry, oocyte cell, optical fibre, pupil function, ray tracing, Zernike mode representation of the wavefront.

Summary

Wavefront aberrations caused by the refractive index structure of the specimen are known to compromise signal intensity and three-dimensional resolution in confocal and multiphoton microscopy. However, adaptive optics can measure and correct specimen-induced aberrations. For the design of an adaptive optics system, information on the type and amount of the aberration is required. We have previously described an interferometric set-up capable of measuring specimen-induced aberrations and a method for the extraction of the Zernike mode content. In this paper we have modelled specimen-induced aberrations caused by spherical and cylindrical objects using a ray tracing method. The Zernike mode content of the wavefronts was then extracted from the simulated wavefronts and compared with experimental results. Aberrations for a simple model of an oocyte cell consisting of two spherical regions and for a model of a well-characterized optical fibre are calculated. This simple model gave Zernike mode data that are in good agreement with experimental results.

Introduction

The methods of confocal and multiphoton microscopy are widely used in the life sciences (Pawley, 1995; Alberts *et al.*, 1999). Optical sections and three-dimensional (3D) images from thick biological specimens can be obtained. A drawback common to these methods is their sensitivity to aberrations. The quantity imaged is the concentration of fluorescent molecules within the specimen. A typical biological object shows additional variations in refractive index, which influence the wavefront as it propagates between the objective lens and the focal region. As a result of the refractive index variations the wavefront deviates from the ideal shape and the optimal, diffraction-limited operation of the instrument is not maintained. The intensity distribution in the focal region is distorted and signal intensity and resolution of the instrument are compromised. Although one could compensate for the loss in signal intensity by an increase in the illumination intensity, this should be avoided because one would like to keep the deposited excitation energy as low as possible to avoid damage to the biological specimen and photobleaching of the dye.

It has been suggested to correct for aberrations of the wavefront using adaptive optics. This principle, initially developed for astronomy (Hardy, 1998), can be applied to confocal microscopy (Booth *et al.*, 2002). The idea is to feed a pre-aberrated wavefront into the optical system that contains aberrations opposite to those generated within the system. The aberrations will therefore cancel out and diffraction-limited imaging is accomplished again. A standard adaptive optics system includes a wavefront sensing element [e.g. Shack–Hartmann sensor; (Platt & Shack, 2001) or modal sensor (Neil *et al.*, 2000)], a wavefront correction element [e.g. deformable mirror or spatial light modulator (SLM)] and works in closed loop operation. In order to design such adaptive optics systems for microscopy we need to assess the aberrations that may occur.

The influence of refractive index mismatch in fluorescence microscopy was first theoretically analysed by Hell *et al.* (1993). The spherical aberration components caused by focusing through layers of mismatched refractive index can be calculated analytically if the refractive index and thickness of each layer is known (Török *et al.*, 1995; Booth *et al.*, 1998). Apart from imaging of layered structures, many biological specimens can be approximated by cylindrical or spherical object shapes (e.g. cells) of uniform refractive index or superpositions of several of these structures.

In this paper we calculate the specimen-induced deformations of the wavefront for spherical and cylindrical objects. The specimen is approximated by cylindrical or spherical regions of uniform refractive index or combinations thereof. A ray tracing method is used to obtain the pupil phase function and subsequently the Zernike mode content of the wavefront employing numerical integration. A mouse oocyte cell and an

Correspondence to: Michael Schwertner. Fax: +44 (0)1865 273905; e-mail: Michael.Schwertner@hertford.ox.ac.uk

optical fibre are modelled and the simulations are compared with experimental results. The interferometer set-up we used for the direct measurements of the specimen-induced aberrations is described in Schwertner *et al.* (2004).

Wavefront aberration simulation for spherical object

The wavefront in the pupil plane of the lens can be described by complex pupil function (Wilson & Sheppard, 1984):

$$P(r,\theta) = A(r,\theta)\exp[i(\psi_0 + \psi(r,\theta))], \qquad (1)$$

where ψ_0 is an arbitrary offset of the phase and $\psi(r,\theta)$ describes the change in phase induced by the specimen. In the ideal, unaberrated case $\psi(r,\theta)$ would be constant. Our model specimen shows variation in refractive index but no absorption. We assume uniform illumination of the pupil, such that the amplitude $A(r,\theta)$ is unity while the phase $\psi(r,\theta)$ varies. The specimen is approximated by a spherical region that has an absolute difference of $\Delta n_1 = n_1 - n_0$ in refractive index between the spherical region (n_1) and the homogenous embedding medium (n_0). It is assumed that the small change in refractive index does not cause deviation of the direction of the traced ray. A schematic diagram of the simulation model is shown in Fig. 1. Here γ represents the half angle of the cone of marginal rays defined by the numerical aperture, $\sin(\alpha)$, of the objective lens. If the virtual specimen were immersed in a substance of refractive index $n_0 = n$, for which the lens has been designed, then $\gamma = \alpha$.

Otherwise, if the specimen were immersed into medium of refractive index $n_0 = n'$, γ would be given by Snell's law: $\gamma = \arcsin(\sin(\alpha)/n')$. The ray being traced is defined by the unit vector $\mathbf{t}$ and the point P through which it passes; β is the inclination angle of the ray to the optical axis (see Fig. 1). The functions $A(r,\theta)$ and $\psi(r,\theta)$ are defined over a normalized pupil of radius $r_{max} = 1$. Assuming the objective lens obeys Abbe's sine condition (Born & Wolf, 1983), the ray is mapped to the radial coordinate of the pupil by $r = \sin(\beta)/\sin(\gamma)$. If the length of the ray section within the sphere is denoted by $a(r,\theta)$, the phase function is given by

$$\psi(r,\theta) = \frac{2\pi}{\lambda}\Delta n a(r,\theta) = \frac{2\pi}{\lambda}\Delta n a(m,t), \qquad (2)$$

where λ is the wavelength and the coordinates (r,θ) in the pupil plane may be expressed in terms of the vectors $\mathbf{m}$ and $\mathbf{t}$ as defined in Fig. 2. The vector $\mathbf{m}$ points from the focus to the centre of the sphere and $\mathbf{t}$ is a unit length direction vector with components:

$$\begin{aligned} t_x &= r\sin(\gamma)\cos(\theta) \\ t_y &= r\sin(\gamma)\sin(\theta) \\ t_z &= \sqrt{[1 - r^2\sin^2(\gamma)]}. \end{aligned} \qquad (3)$$

The value of a, which is the section the ray travels within the sphere, can be calculated from the distance d between the ray and the centre of the sphere by

$$a(m,t) = \begin{cases} 2\sqrt{R^2 - d^2(\boldsymbol{m},\boldsymbol{t})} & \text{for } d < R \\ 0 & \text{otherwise} \end{cases}. \qquad (4)$$

From Fig. 2 we see that $d(\mathbf{m},\mathbf{t})$ follows from

$$d(\boldsymbol{m},\boldsymbol{t}) = |LC| = |\boldsymbol{m} - \boldsymbol{v}| = |\boldsymbol{m} - t(\boldsymbol{m}\cdot\boldsymbol{t})|. \qquad (5)$$

If the vector $\mathbf{m}$ has the components (m_x, m_y, m_z) we obtain:

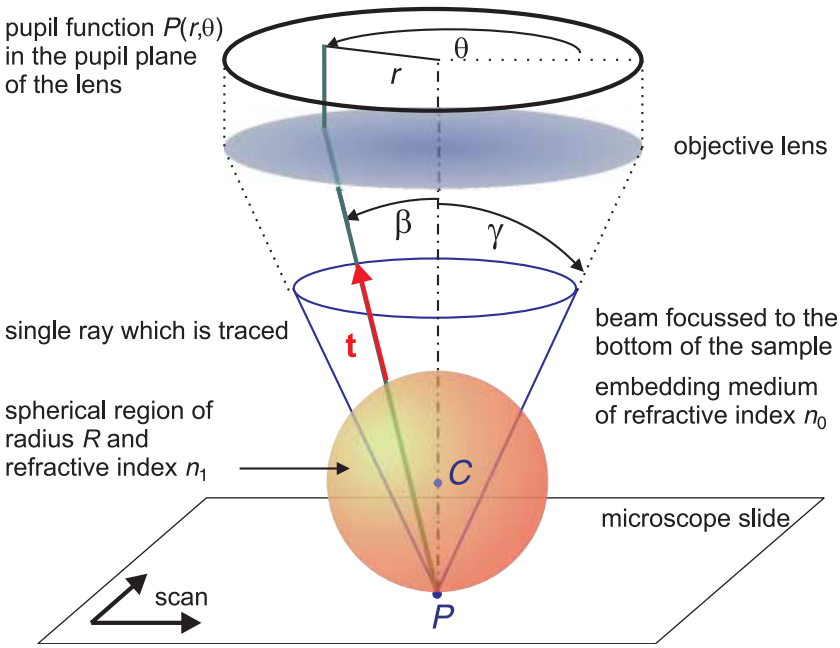

Fig. 1. The model for the calculation of the aberration caused by a spherical object.

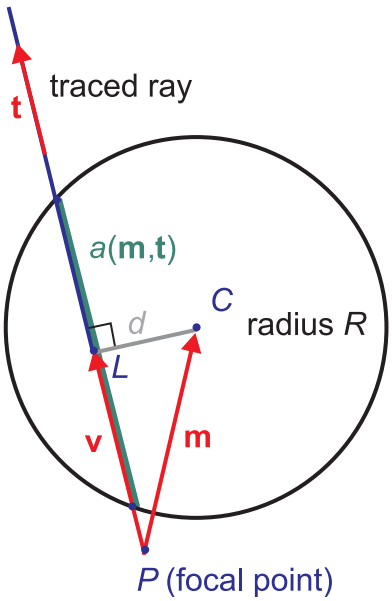

Fig. 2. Illustration of the plane that contains the centre *C* of the sphere and the traced ray passing the focal point *P* in a direction defined by the vector **t**.

$$d^2 = (m_x - t_x(m_x t_x + m_y t_y + m_z t_z))^2 + (m_y - t_y(m_x t_x + m_y t_y + m_z t_z))^2 + (m_z - t_z(m_x t_x + m_y t_y + m_z t_z))^2. \quad (6)$$

Now the phase function $\psi(r,\theta)$ can be calculated using Eqs (2–6). The scanning across the virtual sample may be implemented by altering the coordinates of the centre *C* of the sphere and the focusing depth can be changed by modifying the coordinates of the focal point *P* of the model.

Because the raw phase function itself is hard to interpret, it is useful to represent the phase function of the aberrated wavefront by its Zernike mode content. The Zernike polynomials are a set of orthogonal functions over the unit circle; some of the lower order modes correspond directly to the classic aberration terms as for instance astigmatism and coma. It is also convenient to base correction schemes of adaptive optics systems on Zernike modes because in many cases it is sufficient to correct for a few lower order Zernike modes only. Because of the orthogonality of the polynomials the decomposition of the phase function into Zernike mode amplitudes can be written as:

$$M_i = \frac{1}{\pi}\int_0^1\int_0^{2\pi} \psi(r,\theta) Z_i(r,\theta) r \, d\theta \, dr \quad (7)$$

where $Z_i(r,\theta)$ is the Zernike polynomial of order i and M_i denotes the corresponding amplitude of that mode. For a listing of low-order modes and further references on Zernike polynomials see the Appendix.

Figure 3 displays the simulated Zernike mode variations of the aberrated wavefront while 'scanning' across the virtual spherical sample. The simulations (a) to (c) differ in focusing depth. The plane probed in (a) contains the centre of the sphere and shows the lowest magnitude of aberrations and no tip or tilt are present because of the symmetry conditions for the cone of rays focused to this plane. For an intermediate focal position between centre and bottom (b) and for the bottom focal plane (c) higher aberration magnitudes are found; non-zero values for the tip/tilt modes and slightly changed shapes of some of the Zernike aberration patterns occur.

This simulated sphere could be regarded as a very simple model for a spherical cell within a water-based sample. The model sphere has refractive index of 1.35 and cell cytoplasm has typically refractive index in the range 1.35–1.38 (Dunn, 1998).

Modelling of an oocyte cell and comparison to experimental results

The aberrations caused by a mouse oocyte cell are modelled in order to verify the experimental results obtained by interferometric wavefront measurements. Because this particular type of cell has a basic shape, wavefront simulations can be based on a simple model. The transmitted light image of the cell is shown in Fig. 4 next to the model used for the simulations. The real cell had a diameter of approximately 80 µm and a range of 100 µm was scanned on a 16×16 grid. The simulation calculates the field-dependent component of the aberration only. Additional aberration terms due to the refractive index mismatch between immersion medium and embedding medium are not considered here but have previously been calculated (Török *et al.*, 1995; Booth *et al.*, 1998). The simulation assumed diameters of the two concentric spheres of 80 µm and 52 µm as inferred from a transmitted light image of the cell and used the values for the numerical aperture (dry lens, NA = 0.5) and the 'scanned' field (100 µm × 100 µm) as determined experimentally. The difference in refractive index between embedding medium and the biological specimen could not be determined by complementary methods, but $\Delta n_1 = 0.016$ and $\Delta n_2 = 0.030$ (inner sphere) were found to give good agreement with the experimental data. In the experiment the focus was set to the supposed bottom of the cell with an accuracy of better than 5 µm. A setting of 10 µm above the lower edge of the outer sphere of the simulation was found to give the best reproduction of the experimental data. This could be explained by the fact that the cell is not perfectly spherical and the cross-section in the *z*-direction is smaller than that in the *x*-direction.

Figure 5 shows the simulation and the interferometric wavefront measurement results next to each other. The Zernike mode charts for both the datasets are displayed at the same scale and show the variation of the different modes across the scanned field of view. The experimental set-up uses a phase stepping interferometer in transmission geometry, in which the sample is mounted between two opposing objective lenses contained in the measurement arm of the interferometer. A mirror mounted in the reference path is moved by a piezo

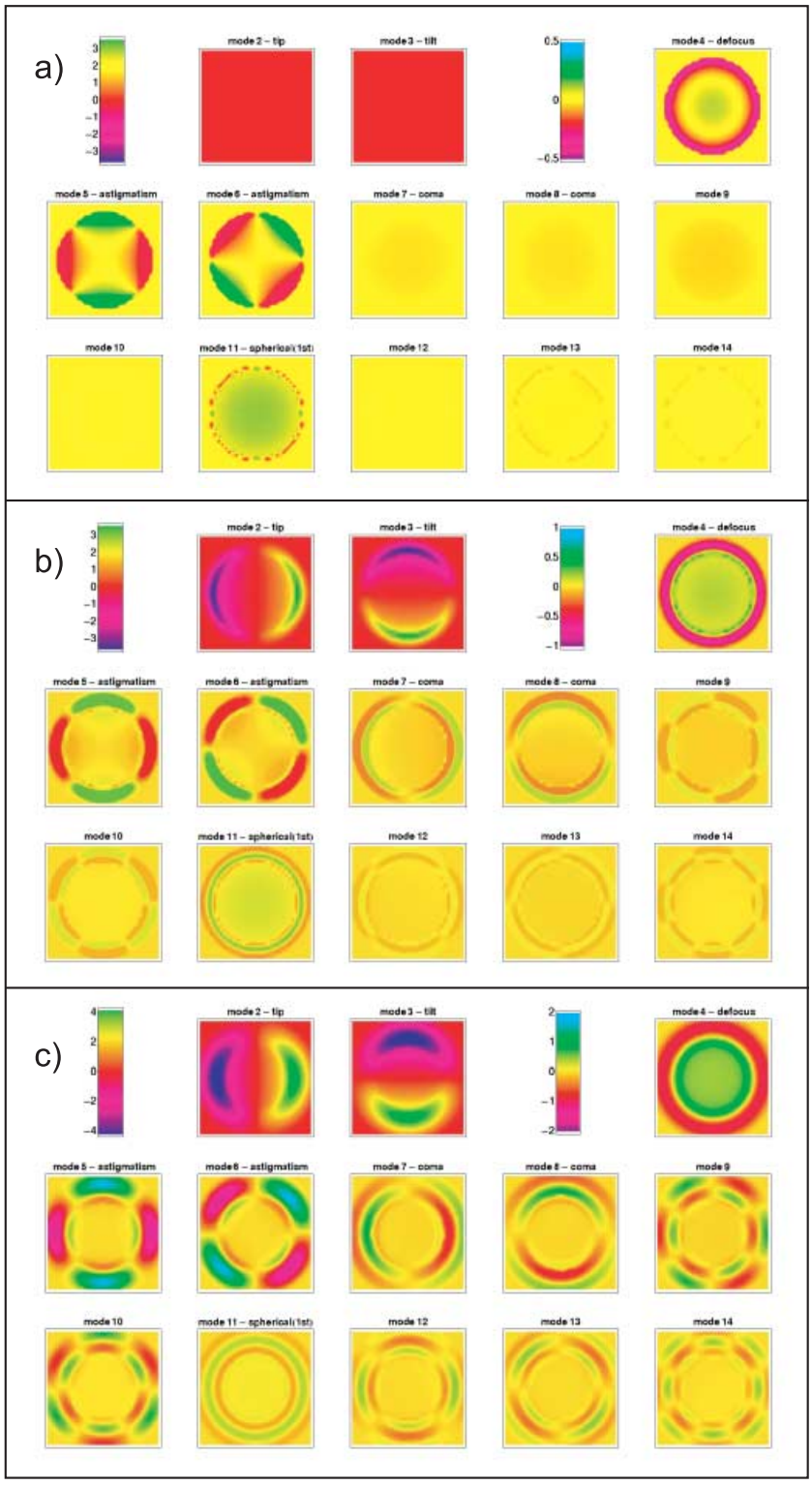

Fig. 3. Simulation of specimen-induced aberrations for a sphere 80 μm in diameter and uniform refractive index $n_1 = 1.35$, embedded in water ($n_0 = 1.33$) and with a dry lens with numerical aperture NA = 0.5. The virtual sample was scanned on a 32×32 grid covering a field of view of 100×100 μm. For each of the grid positions, the wavefront is calculated using the described ray tracing method. Three different focal depths are shown: (a) centre of the cell 40 μm above the bottom, (b) intermediate plane 20 μm above the bottom and (c) bottom of the cell. Note the different scales among the simulations.

actuator and performs phase stepping at videorate. The sample is mounted on an x–y stage and translated perpendicular to the optical axis and wavefronts are recorded on a 16×16 grid across the specimen. For experiment and simulation, Zernike modes 2–22 were extracted from the wavefronts but the figures show modes 2–12 only because the higher order modes have relatively low amplitudes. Note that an adaptive optics aberration correction system would not correct the Zernike

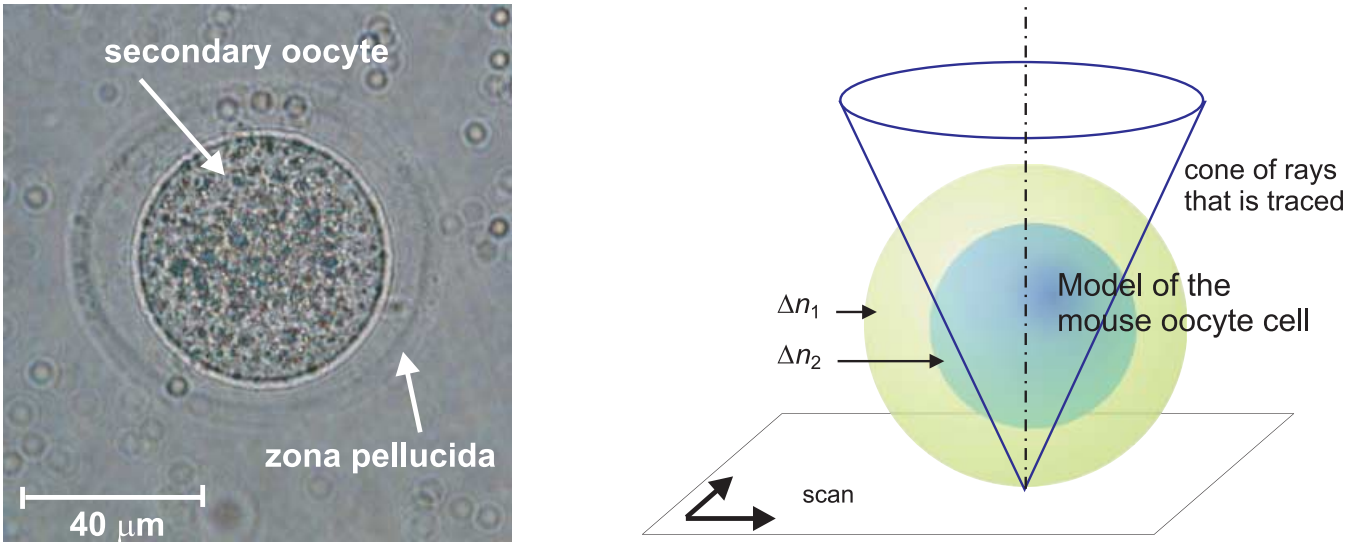

Fig. 4. Transmitted light image of the mouse oocyte cell (left) and the geometric model used for the simulation of wavefront aberrations (right).

modes tip (2), tilt (3) or defocus (4) because these aberration modes correspond to lateral or longitudinal translation of the focal spot but leave signal intensity and resolution unaffected. The presence of these modes in the aberrated wavefront causes geometric distortions in the obtained 3D dataset because there is a difference between the actual and the predicted position of the focal spot. However, correction would require detailed knowledge of the refractive index distribution of the specimen.

Note that the experimental measurement shown in Fig. 5 contains the static aberration component caused by the refractive index mismatch in addition whereas the simulation covers the field-dependent fraction only. The static component mainly affects the mode 11 (first spherical) and causes an additional Zernike amplitude offset for this mode. The agreement between experiment and simulation is good and the main features of the Zernike mode variations across the field are reproduced by the simulations.

Wavefront aberration simulation for cylindrical object

The simulation model for wavefront aberrations of cylindrical objects is very similar to the one we used for spherical objects. Again we would like to find the pupil function $P(r,\theta)$ of Eq. (1) depending on the focal position and the geometry of the specimen. A sketch of the simulation model is depicted in Fig. 6. The unit direction vector $\mathbf{w}$ defines the direction of the cylinder axis, C is a point on the cylinder axis, R denotes the radius and $\Delta n_c = n_c - n_0$ is the absolute difference in refractive index of the cylinder with respect to the immersion medium. The unit direction vector $\mathbf{t}$ again describes the direction of the traced ray and is obtained from the polar coordinates of the pupil plane using Eq. (4). The vector denoted by $\mathbf{m}$ points from the focus to the cylinder axis. If $a(\boldsymbol{m},\boldsymbol{t},\boldsymbol{w})$ denotes the distance the ray travels within the cylinder, we find

$$a(m,t,w) = \begin{cases} 2\sqrt{R^2 - d^2(\boldsymbol{m},\boldsymbol{t},\boldsymbol{w})} & \text{for } d < R. \\ 0 & \text{otherwise} \end{cases} \tag{8}$$

Here $d(\mathbf{m},\mathbf{t},\mathbf{w})$ refers to the distance between the passing ray and the axis of the cylinder. If, furthermore, the vector $\mathbf{w}$ is normalized to unity, the distance d is given by

$$d(m,t,w) = \frac{|\boldsymbol{m} \cdot (\boldsymbol{w} \times \boldsymbol{t})|}{|\boldsymbol{w} \times \boldsymbol{t}|}. \tag{9}$$

Using the vector components we obtain

$$d(\boldsymbol{m},\boldsymbol{t},\boldsymbol{w}) = \sqrt{\frac{(m_x(w_y t_z - w_z t_y))^2 + (m_y(w_z t_x - w_x t_z))^2 + (m_z(w_x t_y - w_y t_x))^2}{(w_y t_z - w_z t_y)^2 + (w_z t_x - w_x t_z)^2 + (w_x t_y - w_y t_x)^2}}. \tag{10}$$

Now Eqs (2), (4) and (10) allow us to calculate the phase function that contains the aberration due to the wavefront distortions imposed by the object.

Optical fibre simulation and comparison to experimental results

An optical fibre has a defined geometry and a well-known refractive index. Therefore, it is ideal for wavefront aberration experiments and corresponding simulations. For the experiments we chose a multimode fibre composed of fused silica. The polymer fibre jacket was carefully stripped off using a scalpel and the remaining glass fibre was mounted in immersion oil (Zeiss, $n_0 = 1.518$ at 23 °C). A transmitted light image of the fibre is shown in Fig. 7; its outer diameter was measured to be 71 μm. The refractive index of fused silica at the used

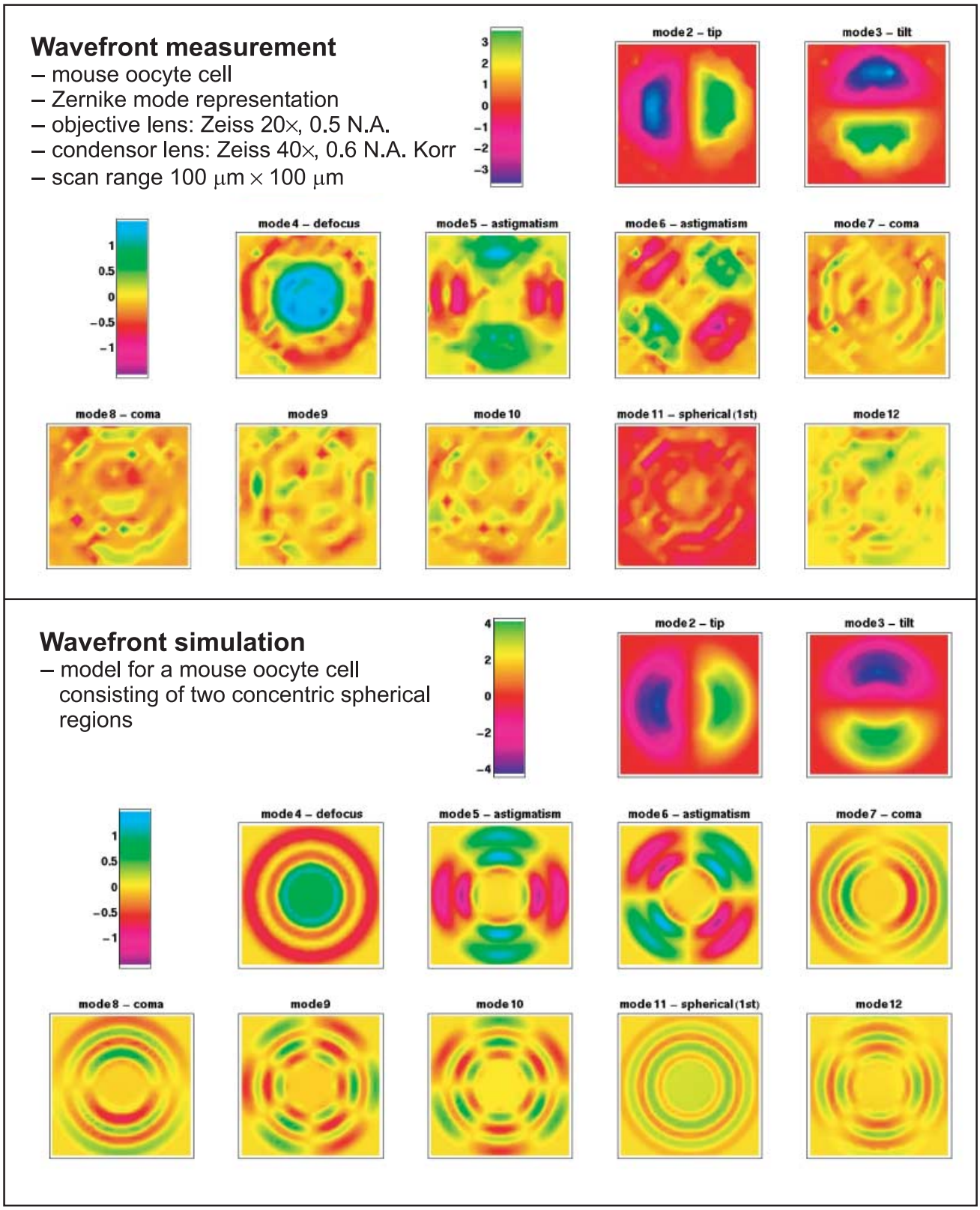

Fig. 5. Variation of the Zernike mode amplitudes of the aberrated wavefront across the field of view. Experimental results for the wavefront measurements of a mouse oocyte cell (top) and corresponding simulation results (bottom). In the experiment, the specimen was translated and wavefronts were recorded on a grid of 16 × 16 points across the specimen. For the simulation, four times the number of data points were calculated on a 32 × 32 grid.

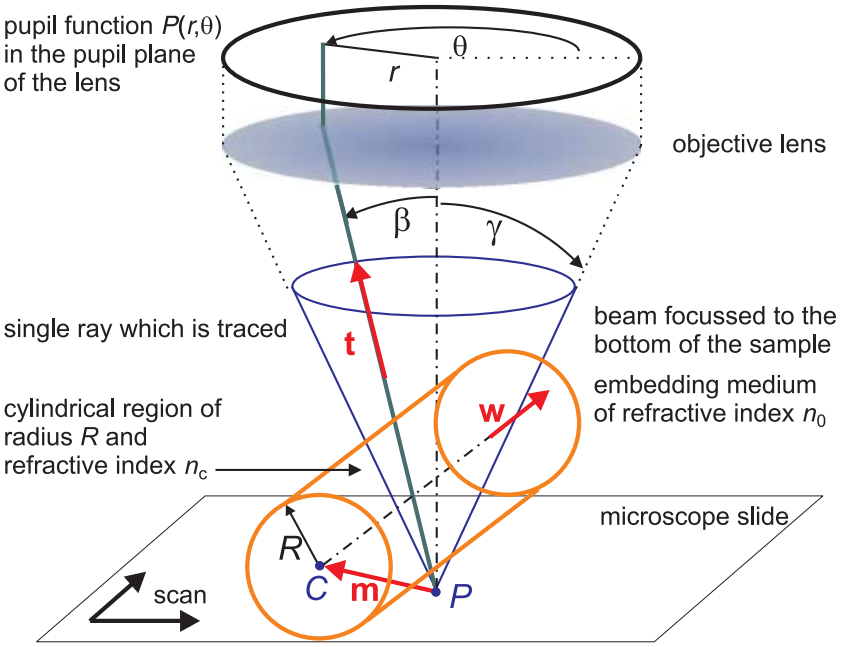

Fig. 6. Model for the calculation of the aberrations caused by a cylindrical object.

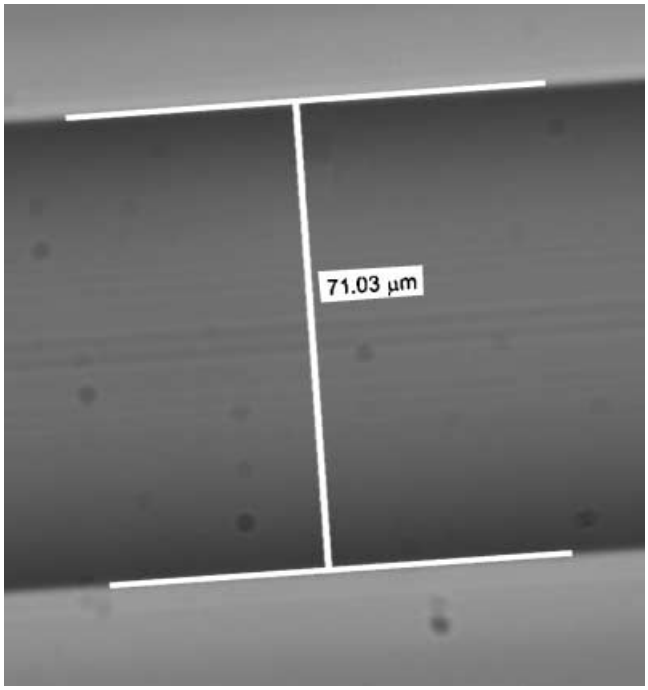

Fig. 7. Transmitted light microscope image of the optical fibre used for the interferometric wavefront measurements. A measurement bar indicates the diameter; this value was used for the simulations.

wavelength of 632.8 nm (HeNe Laser) is 1.49, and thus the refractive index difference is expected to be $\Delta n_c = -0.028$. The wavefront measurement and subsequent Zernike mode extraction were performed using Eq. (7). Again details on data acquisition and the set-up can be found in Schwertner *et al.* (2004).

The experimental results and the corresponding simulations are shown in Fig. 8. Because the condenser lens was equipped with a correction collar, it was feasible to compensate for the remaining static fraction of the aberration due to the refractive index mismatch. This occurs because a dry lens was used to focus into an oil-based sample. As result of this compensation adjustment, the experimental data contain the field-dependent part of the aberration only.

For the simulations, the refractive index difference of $\Delta n_c = -0.028$, the refractive index of the immersion medium $n_0 = 1.518$, the measured fibre diameter of 71 µm, the position of the focal spot was 15 µm below the bottom of the fibre, the numerical aperture NA = 0.5, and a field of view of 130 µm were used as the parameters of the experiment. The core of the optical fibre is visible in Fig. 7. It is not included in the simulations because this doped region has only small difference in refractive index and the core volume can be neglected compared to the volume of the whole fibre.

The experimental results for the fibre simulation are shown in the lower part of Fig. 8 and agree well with the experimental results. The main features of the measured Zernike mode variations across the field of view are reproduced by the simulation. There are deviations from the simulation for some modes in the top left-hand corner of the fibre (for instance visible in mode 5). This was due to total internal reflection effects close to the edge of the fibre, which caused a deflection of intensity out of the pupil, which in turn triggered problems for the Zernike mode fitting for these particular wavefronts. Only very few data points of the experimental data were affected because the fibre was not horizontally aligned, only a very narrow range of positions in respect to the fibre axis show the effect

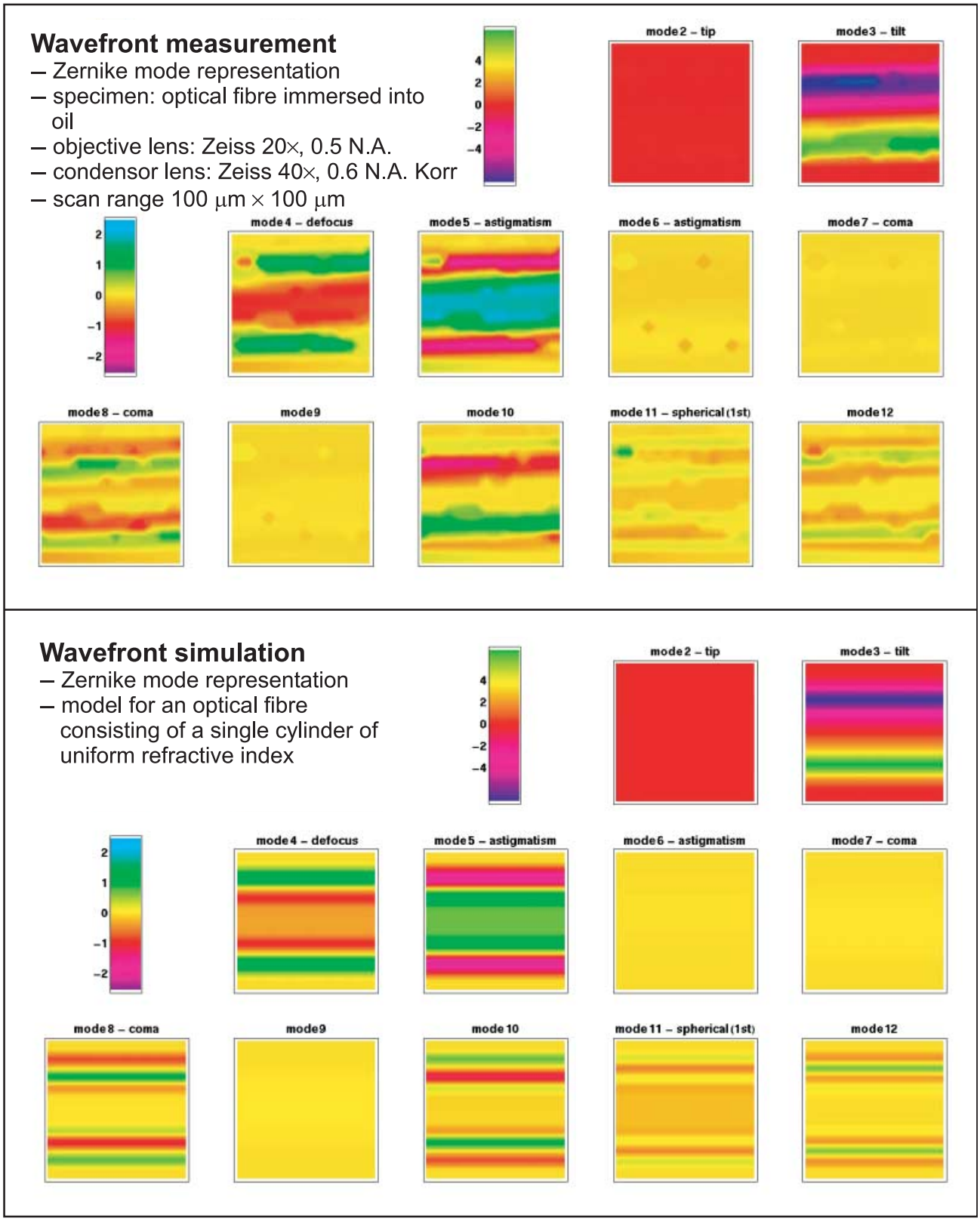

Fig. 8. An optical fibre specimen. Representations of the Zernike mode amplitudes of the aberrated wavefront when the optical fibre is imaged. Top: experimental results from the interferometric wavefront measurements; bottom: simulation results for a cylinder of uniform refractive index ($n_c = 1.49$) embedded in oil ($n_0 = 1.518$).

and wavefront measurements were recorded on a rather coarse grid corresponding to steps of about 9 μm.

Discussion and conclusions

Ray tracing simulations of the specimen-induced aberrations caused by cylindrical and spherical objects were performed. Simulation examples for focusing into a spherical object at different depths were given. A sphere of refractive index 1.35 immersed into water can be regarded as a very simple model of a cell within a water-based sample. Note that the simulations are carried out for a wavefront that is propagating through the whole sample – as this is the case for our interferometric wavefront measurement set-up. A confocal microscope works in epi-mode and the fluorescence excitation and emission beams propagate between the objective lens and the focal spot only. Therefore, the simulation results are strictly equivalent to the epi-mode only when the focus is set to the bottom or top of the sample.

Simulations for a mouse oocyte cell and an optical fibre were calculated and compared with experimental results obtained by interferometric wavefront measurements. The Zernike mode data from the ray tracing are in good agreement with the measured experimental data for both the modelled samples; the characteristic features of the Zernike amplitude distribution across the field of view were reproduced by the simulation. Furthermore, approximations for the difference in refractive index between the biological cell and the embedding medium and the focal position were inferred from the simulation as a result of the best approximation found for the experimental data.

Again the simulations showed that the aberrations can be described by a relatively small number of Zernike modes. This means that it is sufficient in adaptive optics systems to correct for a small number of modes only.

A limitation of the current ray tracing model is the assumption of straight propagation of the rays. This approximation holds for small and rather smooth variations in the refractive index and is justified for the samples under investigation. The relative differences in refractive index of about 2% were rather small but values of that magnitude are expected for biological samples embedded in water-based solutions. Further experiments and simulations, also for high-NA lenses, will confirm whether this simplification of the model holds for all relevant samples.

Acknowledgements

We would like to thank Richard Gardner and Tim Davis, Department of Zoology, Oxford, for the preparation of the mouse oocyte sample. This work was supported by Carl Zeiss Jena GmbH. M.S. is grateful for a grant from the DAAD Germany (Deutscher Akademischer Austauschdienst).

References

Alberts, B., Bray, D., Lewis, J., Raff, M., Roberts, K. & Watson, J.D. (1999) *Molecular Biology of the Cell*, 3rd edn. Garland Publishing, New York.

Booth, M.J., Neil, M.A.A., Juškaitis, R. & Wilson, T. (2002) Adaptive aberration correction in confocal microscope. *Proc. Natl Acad. Sci. USA*, **99**, 5788–5792.

Booth, M.J., Neil, M.A.A. & Wilson, T. (1998) Aberration correction for confocal imaging in refractive-index-mismatched media. *J. Microsc.* **192**, 90–98.

Born, M. & Wolf, E. (1983) *Principles of Optics*, 6th edn. Pergamon Press, Oxford.

Dunn, A. (1998) *Light scattering properties of cells*. Dissertation, University of Texas, Austin. http://www.nmr.mgh.harvard.edu/~adunn/papers/dissertation /node7.html.

Hardy, J.W., (1998) *Adaptive Optics for Astronomical Telescopes*. Oxford University Press, Oxford.

Hell, S., Reiner, G., Cremer, C. & Stelzer, E.H.K. (1993) Aberrations in confocal fluorescence microscopy induced by mismatches in refractive index. *J. Microsc.* **169**, 391–405.

Neil, M.A.A., Booth, M.J. & Wilson, T. (2000) New modal wavefront sensor: a theoretical analysis. *J. Opt. Soc. Am.* **17**, 1098–1107.

Noll, R.J. (1976) Zernike polynomials and atmospheric turbulence. *J. Opt. Soc. Am.* **66**, 207–277.

Pawley, J.B. (1995) *Handbook of Biological Confocal Microscopy*. Plenum Press, New York.

Platt, B.C. & Shack, R. (2001) History and priciples of Shack–Hartmann wavefront sensing. *J. Refractive Surg.* **17**, 573–577.

Schwertner, M., Booth, M., Neil, M.A.A. & Wilson, T. (2004) Measurement of specimen-induced aberrations of biological samples using phase stepping interferometry. *J. Microsc.* **213**, 11–19.

Török, P., Varga, P. & N'emeth, G. (1995) Analytic solution of the diffraction integrals and interpretation of wave-front distortion when light is focussed through planar interface between materials of mismatched refractive indices. *J. Opt. Soc. Am.* **12**, 2660–2671.

Wilson, T. & Sheppard, C.J.R. (1984) *Theory and Practice of Scanning Optical Microscopy*. Academic Press, London.

Appendix: Zernike polynomials

Table A1 below lists the Zernike polynomials 2–14 that were used for the wavefront analysis throughout this paper employing Eq. (7). Here we prefer a single indexing scheme, but a double indexing scheme (n, m radial and azimuthal) can be found in the literature as well. Both versions are listed. For more information on Zernike polynomials see Noll (1976), Born & Wolf (1983) and Schwertner *et al.* (2004).

Table A1. Zernike polynomials 2–14 used for the wavefront analysis via Eq. (7).

i	n	m	$Z_n^m(r,\theta)$	Aberration term
1	0	0	1	piston
2	1	1	$2r\cos(\theta)$	tip
3	1	−1	$2r\sin(\theta)$	tilt
4	2	0	$\sqrt{3}(2r^2-1)$	defocus
5	2	2	$\sqrt{6}\,r^2\cos(2\theta)$	astigmatism
6	2	−2	$\sqrt{6}\,r^2\sin(2\theta)$	astigmatism
7	3	1	$2\sqrt{2}(3r^3-2r)\cos(\theta)$	coma
8	3	−1	$2\sqrt{2}(3r^3-2r)\sin(\theta)$	coma
9	3	3	$2\sqrt{2}\,r^3\cos(3\theta)$	
10	3	−3	$2\sqrt{2}\,r^3\sin(3\theta)$	
11	4	0	$\sqrt{5}(6r^4-6r^2+1)$	spherical (1st)
12	4	2	$\sqrt{10}(4r^4-3r^2)\cos(2\theta)$	
13	4	−2	$\sqrt{10}(4r^4-3r^2)\sin(2\theta)$	
14	4	4	$\sqrt{10}\,r^4\cos(4\theta)$	